Talanta 179 (2018) 145–152

Contents lists available at ScienceDirect

Talanta

journal homepage: www.elsevier.com/locate/talanta

# Fabrication of novel superoxide anion biosensor based on 3D interface of mussel-inspired $Fe_3O_4$-$Mn_3(PO_3)_2$@Ni foam

Qi Wang[a], Qian Zhou[a], Qicheng Zhang[a], Rongjia Shi[a], Shangshang Ma[a], Wenbo Zhao[a,*], Min Zhou[b,*]

[a] National and Local Joint Engineering Research Center of Biomedical Functional Materials, Jiangsu Key Laboratory of Biofunctional Materials, School of Chemistry and Materials Science, Nanjing Normal University, Nanjing 210023, China
[b] Department of Vascular Surgery, Nanjing Drum Tower Hospital, The Affiliated Hospital of Nanjing University Medical School, Nanjing 210000, China

ARTICLE INFO

*Keywords:*
3D biosensor
Nickel foam
Mussel-inspired
Bionic enzyme
Cell adhesion
Superoxide anion detection

ABSTRACT

Preparation of high performance electrochemical biosensing interface for the sensitive and rapid detection of human metabolites is of great interest for health care and biomedical science. In this paper, based on the adhesion technique of marine mussels, we designed and prepared a novel biosensor with a micro/nano-biointerface of $Fe_3O_4$-$Mn_3(PO_3)_2$@Ni foam, which offered a three dimensional (3D) living environment for real cell. The constructed biosensor with a 3D micro/nano-biointerface of $Fe_3O_4$-$Mn_3(PO_3)_2$@Ni foam was characterized by scanning electron microscopy (SEM), energy dispersive spectroscopy (EDS) and elemental mapping. Furthermore, the electrochemical experiments by electrochemical method for detection of superoxide anion ($O_2^{\bullet -}$) in situ released by cells were carried out by this biosensor we proposed. Results indicated that the 3D interface of mussel-inspired $Fe_3O_4$-$Mn_3(PO_3)_2$@Ni foam offered an amicable platform for promoting cell adhesion, which was beneficial for enhancing biosensing activity. This proposed sensing platform provided high electroactivity and excellent electron transport with a lower detection limit (0.0170 μM), wider linear range 0.04–2.44 μM) and short diffusion distance to reaction sites. The case achieved the accurate detection of $O_2^{\bullet -}$ (in situ released by cells) based on the combination of mussel-inspired biomimetic adhesion technique, 3D micro/nano-biointerface construction and electrochemical biosensing technique.

## 1. Introduction

Superoxide anions ($O_2^{\bullet -}$), as a typical type of reactive oxygen species (ROS), is produced by organism deviating from the usual standards, which may lead to a higher incident rate of cancer risk, an accelerated aging and some forms of neural degeneration with irreversible consequences such as Parkinson's disease [1–5]. Therefore, it is of vital importance to find a suitable method that can detect $O_2^{\bullet -}$ reliably, promptly, and explicitly, which is supposed to be easy to implement and suitable for routine diagnosis, pathological analysis, and operation for daily physical examination.

Among the various methods developed for detection $O_2^{\bullet -}$ thus far [6–8], electrochemical method, with the advantages of fast response, simple operation and high sensitivity [9–14], has been received wide attention. Amperometric enzyme electrodes for $O_2^{\bullet -}$ have been developed with various electrode materials, such as cytochrome c and superoxide dismutase (SOD) [15–17]. However, enzyme-based biosensors were difficult to be used widely owing to the inherent weaknesses of the enzyme, such as high volatility, high cost, and difficulty in storage. One of the most promising materials is manganese (Mn) compound as the biomimetic enzyme that takes advantage of catalytic dismutation of $O_2^{\bullet -}$ [18]. Silica-manganese phosphate ($SiO_2$-$Mn_3(PO_4)_2$) nanoparticles were synthesized by surface self-assembly processes for $O_2^{\bullet -}$ detection as reported in our previous work [19].

Until now, most of cytosensors for detection of cellular molecules in situ were based on a two dimensional (2D) detected platform that utilized to capture the detected cells. In fact, real cells inhabit a three dimensional (3D) space with complicated microenvironment [20–23]. So if a simulating real 3D environment can be offered for the detected cells, it will facilitate the authenticity and accuracy of cell electrochemical detection. 3D nickel foam has attracted increasing attentions due to its unique 3D scaffold structure, low cost, good magnetic and conductivity [24,25].

In this work, 3D nickel foam was introduced to create a simulating real 3D environment for rapid and accurate detection of $O_2^{\bullet -}$ from detected cells. Firstly, magnetic manganese phosphate nanoparticles

* Corresponding authors.
*E-mail addresses:* zhaowenbo@njnu.edu.cn (W. Zhao), zhouminnju@126.com (M. Zhou).

http://dx.doi.org/10.1016/j.talanta.2017.10.054
Received 15 August 2017; Received in revised form 18 October 2017; Accepted 25 October 2017
Available online 02 November 2017
0039-9140/ 

($Fe_3O_4$-$Mn_3(PO_4)_2$ NPs) synthesized by surface self-assembly technology were directly and robustly anchored on 3D nickel foam based on the mussel-inspired adhesion technique. Then, this 3D nickel foam was attracted by magnetic electrode to construct a novel biosensor with 3D interface for $O_2^{\bullet-}$ detection. The as-obtained biosensor, based on a 3D micro/nano-biointerface as an amicable platform to promote cells adhesion, could not only greatly shorten detection cycle and simplify test process, but also shorten the diffusion distance between $O_2^{\bullet-}$ released from cell and the medium solution for enhanced sensing performance. This biosensor provided a new opportunity for the design and application of 3D electrode materials with enhanced electrocatalytic performance in biosensing.

## 2. Experimental section

### 2.1. Materials

Ferric chloride hexahydrate ($FeCl_3{\cdot}6H_2O$) and tetraethyl orthosilicate (TEOS) were purchased from Sinopharm Chemical Reagent Co. Ltd. Sodium acetate (NaAc) was obtained from Shanghai Lingfeng Chemical Reagent Co. Ltd. (3-Aminopropyl) triethoxysilane (APTES), phytic acid (PA, 70 wt%) solution and phytic acid sodium salt hydrate were purchased from Aladdin Chemistry Co. Ltd (Shanghai, China). Manganese sulfate monohydrate ($MnSO_4{\cdot}H_2O$), ethylene glycol (EG), dimethyl sulfoxide (DMSO) were obtained from Sinopharm Chemical Reagent Co. Ltd. Potassium hyperoxide ($KO_2$) was purchased from Alfa Aesar. Triton X-100, 18-crown-6, phorbol 12-myristate 13-acetate (PMA), dopamine hydrochloride (DA), cysteine (Cys), ascorbic acid (AA) and uric acid (UA) were acquired from Aladdin Sigma-Aldrich Co. (USA). Hydrogen peroxide ($H_2O_2$, 30%) was purchased from Beijing Chemical Works (Beijing, China). 3-(4,5-Dimethylthiazol-2-yl)-2,5-diphenyltetrazolium bromide (MTT), dulbecco's modified eagle medium (DMEM), fetal bovine serum (FBS), and penicillin/streptomycin (P/S), 4′,6-diamidino-2-phenylindole (DAPI) were purchased from Nanjing Heyao Biotech. Co., Ltd. (Nanjing, China). Ni foam was purchased from Wuzhou Sanhe New Mater Co., Ltd. (Guangxi, China).

### 2.2. Preparation of $Fe_3O_4$ NPs

The $Fe_3O_4$ NPs were synthesized in accordance with the procedure described in the literature and functionalized via solvothermal route [26–29]. 4.04 g $FeCl_3{\cdot}6H_2O$ was dissolved in 100 mL EG to form a clear solution in a three-necked flask, then 8.20 g NaAc was added quickly under constant and vigorous stirring for 0.5 h. The obtained solution was subsequently moved to a Teflon-lined autoclave (50 mL) that was sealed for 8 h with heating to 200 °C, and then naturally cooled down to room temperature. The resulting black precipitate was got via centrifugation, washed repeatedly with distilled water and absolute ethanol, and dried at 50 °C inside a vacuum oven for 5 h.

### 2.3. Preparation of $Fe_3O_4$-$Mn_3(PO_3)_2$ NPs

$Fe_3O_4$-$Mn_3(PO_3)_2$ NPs fabricated with layer-by-layer (LBL) self-assembly strategy [30–32] exhibited size-controlled (Scheme 1A). First, 0.10 g of $Fe_3O_4$ NPs were ultrasonically treated with 50 mL, 0.1 M HCl aqueous solution for 10 min. Afterwards, the magnetite particles were isolated, and washed with deioned water, and then homogeneously dispersed in a mixture solution (80 mL ethanol, 20 mL deioned water, and 1.0 mL, 28 wt% ammonia), to which TEOS (0.144 mM) was subsequently added. After the mixture had been stirred at room temperature for 6 h, an appropriate amount of APTES was added to it to form the $Fe_3O_4$-$NH_2$ NPs solution in Scheme 1A (a). After the solution had been stirred for 30 min, 120 μL of PA/PA sodium salt hydrate buffer solution (pH = 7) was injected into in under incessant stirring for 24 h. The resulting NPs were washed with alcohol and double-distilled water (Scheme 1A(b)).

Finally, the $Fe_3O_4$-PA NPs were redispersed in 10 mL of water, and then 10 mL of $MnSO_4$ solution (12 mM) were injected to the round-bottomed flask containing $Fe_3O_4$-PA NPs under constant stirring for 1 h at 60 °C. At the end of the reaction, the obtained materials were collected via centrifugation, washed with double-distilled water, and dried in a vacuum oven at 60 °C for 24 h (Scheme 1A(c)).

### 2.4. Preparation of $Fe_3O_4$-$Mn_3(PO_3)_2$@Ni foam

$Fe_3O_4$-$Mn_3(PO_3)_2$ NPs were anchored onto Ni foam in an aqueous solution of dopamine in Scheme 1B (a), which was inspired by the bioadhesion of marine mussels [33,34]. Briefly, 100 mg of $Fe_3O_4$-$Mn_3(PO_3)_2$ NPs and 40 mg of dopamine hydrochloride were dispersed in 20 mL of $H_2O$ at pH = 9 by ultrasonication. The pH of the dispersions was adjusted by NaOH. Then a piece of Ni foam was immersed in the above dispersions under stirring for 12 h. After it was rinsed with water and dried at 80 ℃, the foam covered with as-papered samples was obtained a 3D micro/nano-biointerfaces for further cells adhesion (Scheme 1B(b)).

### 2.5. Preparation of superoxide anion

Dissolving $KO_2$ to DMSO which contained 18-crown-6, a stabilized $O_2^{\bullet-}$ solution was attained. According to the molar absorptivity of $O_2^{\bullet-}$ in DMSO, the concentration of $O_2^{\bullet-}$ was supervised by minuting the deoxidation at 550 nm using ferricytochrome c spectrophotometrically [35].

### 2.6. Culture of cells

The A549 cells were grown at 37 °C in 5% $CO_2$ culture medium with DMEM, 10% fetal bovine serum and 1% P/S. The pretreated cells, gathered by centrifugation, was added into the PBS solution including 100 μg $mL^{-1}$ PMA and 50 mM glucose.

### 2.7. MTT assays

The viable cells viabilities of the $Fe_3O_4$-$Mn_3(PO_4)_2$@Ni foam for different incubation time were appraised using MTT assays. A549 Cells, at a density of $0.5\times10^5$ cells, and synthesized $Fe_3O_4$-$Mn_3(PO_4)_2$@Ni foams were seeded in a 96-well plate for 4 h, 12 h, 24 h incubation period. After then, the wells were treated with 50 μL MTT (2 mg $mL^{-1}$) and incubated for another 4 h at 37 °C. The medium was then displaced with 150 μL of DMSO, and a microplate reader was carried out by monitoring the absorbance at a 570 nm.

### 2.8. Cell capture experiments

1 mL of $5 \times 10^4$ cells suspension was seeded onto a 24-well plate with the different samples. After 60 min incubation time at 37 ℃, the samples were rinsed with PBS for three times. The captured cells on the substrates were fixed with 2.5% GA in PBS for 4 h. The substrate was subsequently dehydrated with in a series of ethanol gradient solution with different volume fractions (30%, 50%, 70%, 90% and 100%) at each concentration for 20 min, and finally dried at room temperature to observe the morphology of the cells on the samples by SEM.

After 4 h fixed treatment with 2.5% GA, the films were covered with a DAPI solution (2 μg $mL^{-1}$) for 15 min, followed by PBS washed. At last, the samples were kept at 4 ℃ in dark for the subsequent fluorescence microscope.

### 2.9. Apparatus and electrochemical measurements

The morphologies of the as-prepared samples were detected by TEM and high-resolution transmission electron microscopy (HITACHI H-7650, Japan). FTIR of the sample were performed from a VARIAN Cary

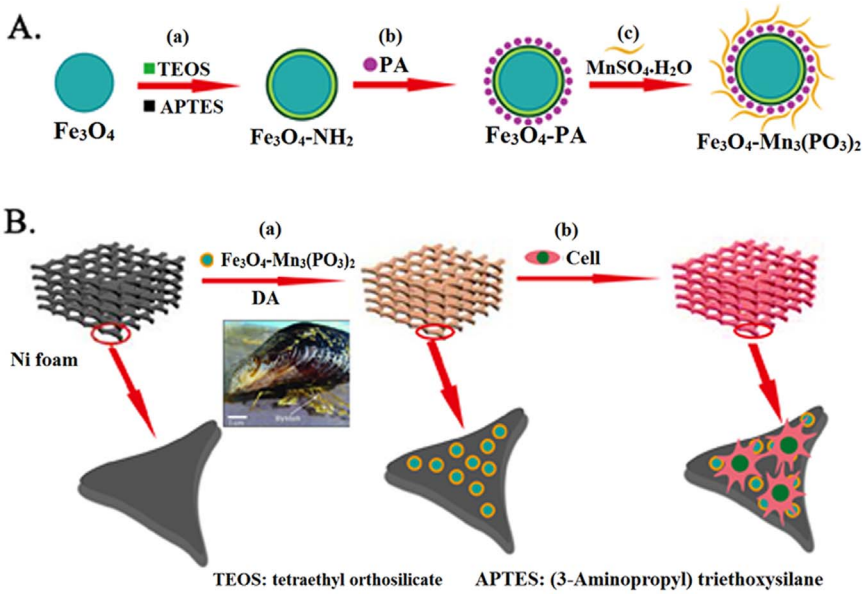


**Scheme 1.** Illustration for (A) the preparation of $Fe_3O_4$-$Mn_3(PO_4)$ NPs: (a) the formation process of $Fe_3O_4$-$NH_2$ NPs, (b) the Phytic acid modified procedure to obtain the $Fe_3O_4$-PA NPs and (c) self-assembly preparation of dropping into $Mn^{2+}$ on the outer surface of $Fe_3O_4$-PA NPs; (B) the construction process of the 3D biosensor: (a) the immobilization process of $Fe_3O_4$-$Mn_3(PO_4)$ NPs onto Ni foam and (b) the A549 cell-adhesion on $Fe_3O_4$-$Mn_3(PO_4)$ NPs@Ni foam.

5000 Fourier transform infrared spectrophotometer (VARIAN, USA). Zeta potential analyzer (Malvern Instruments ZS90) was employed to test surface potential of the NPs. MGCE was obtained from Tianjin Incole Technology Company. All the electrochemicals data, using a three-electrode cell equipped (saturated calomel electrode (SCE), a platinum electrode and working electrode), were measured by electrochemical workstation (CHI 760D, Shanghai Chenhua, China). MTT assays were measured by a microplate reader (Multiskan FC).

The electrochemical properties of $Fe_3O_4$-$Mn_3(PO_4)_2$@Ni foam-MGCE were evaluated using cyclic voltammograms (CV) in the working potential range of −0.3–0.9 V at 100 mV $s^{-1}$ and electrochemical impedance spectroscopy (EIS) by frequency range (1–$10^5$ Hz) and amplitude (0.005 V) in a 0.1 M PBS solution [36–41]. Both selectivity and anti-interference ability of the developed biosensor were assessed against various interfering species. The proposed 3D hybrid biosensor was further investigated for their ability in detecting in situ released $O_2^{\bullet -}$ from A549 cells.

## 3. Results and discussion

### 3.1. The characterization of 3D hybrid foam

The proposed surface self-assembly method makes it possible to synthesize high specific surface area magnetic nanoparticles ($Fe_3O_4$-$Mn_3(PO_4)_2$ NPs) with a controllable shape on the nanoscale. As shown in the TEM image (Fig. S1A, a, ESI), $Fe_3O_4$ NPs had an average diameter of 290 nm. When APTES and PA molecules were adsorbed to the surface of $Fe_3O_4$ particles due to the strong electrostatic interaction, and sequentially $Mn^{2+}$ ions were self-assembled in above solution, the diameter of $Fe_3O_4$-PA NPs and $Fe_3O_4$-$Mn_3(PO_4)_2$ NPs was almost unchanged (Fig. S1B, b and S1C, c, ESI). Compared with the surface of pure Ni foam (Fig. 1A), $Fe_3O_4$-$Mn_3(PO_4)_2$ NPs densely and homogenously deposited onto 3D Ni foam surface (Fig. 1B), indicating immobilizated directly nanoparticle to the foam skeleton by adhesion of dopamine. From Fig. 1C, D, it was clearly observed a multilayer sheet-structured (above 3–5 nm) of the nanoparticles surface. According to the mapping analysis results, iron (Fe) was situated in the particle core while silicon (Si), phosphorus (P), and manganese (Mn) were distributed evenly in the exterior of the particles (Fig. 1E). The EDS spectrum (Fig. S2, ESI) also showed the presence of Fe, Si, P and Mn, which was consistent with the mapping analysis results. The mass weight of Mn element in the EDS result was calculated to be 0.46%, which was confirmed the presence of the self-assembly multilayer layer on the exterior surface of the $Fe_3O_4$-PA NPs.

The well-defined diffraction spots in the selected area electron diffraction (SAED) patterns (Fig. 2A) confirmed the crystallinity of as-prepared $Fe_3O_4$-$Mn_3(PO_4)_2$ NPs, which can be derived potentially from the reflection of five crystal planes of (220), (311), (400), (422), (511) and (440), respectively [42], reflecting that preserved the crystal features of $Fe_3O_4$ NPs. The Zeta potential values (Fig. 2B) were measured to be −20.3, 4.1, −8.62, and −1.27 mV, respectively, for the as-prepared $Fe_3O_4$, $Fe_3O_4$-$NH_2$, $Fe_3O_4$-PA, $Fe_3O_4$-$Mn_3(PO_4)_2$, revealing powerfully self-assembly process of layer by layer. After modified with APTES, the Zeta potential of $Fe_3O_4$-$NH_2$ NPs increased from −20.3 mV to 20.1 mV, which was attributed to the amine groups from APTES adsorbed into the surface of $Fe_3O_4$ NPs containing many -OH groups. Owing to the six phosphate groups of PA, the Zeta value of $Fe_3O_4$-PA NPs showed a negative charge. The Zeta potential increased to −1.27 mV when $Mn^{2+}$ ions in solution were anchored onto the surface of $Fe_3O_4$-PA NPs in a self-assembled manner [19,43,44]. The slightly switch of the diameter from $Fe_3O_4$ to $Fe_3O_4$-$Mn_3(PO_4)_2$ denoted the validity of electrostatic interactions in shaping the $Fe_3O_4$-$Mn_3(PO_4)_2$ NPs. The chemical compositions of various samples was identified by FTIR. As shown in the FTIR spectrum (Fig. 2C), the characteristic peak at around 560 $cm^{-1}$ was the Fe-O group for $Fe_3O_4$ NPs [45]. The curve of $Fe_3O_4$-$NH_2$ NPs illustrated characteristic spectral bands whose formation was attributed to the stretching vibration of -C-$NH_2$ (2920 $cm^{-1}$), the symmetric stretching of -$NH_2$ (1611 $cm^{-1}$), the bending vibrations of -$NH_2$ in APTES (789 $cm^{-1}$), all of which proved that $Fe_3O_4$ NPs were indeed modified by APTES as a consequence of the processes mentioned above [46,47]. Furthermore, according to the adsorption value (1098 $cm^{-1}$) in the curve of $Fe_3O_4$-PA NPs, the phosphate of PA was converged characteristic peaks of asymmetric stretching vibration of the O-Si-O [48]. Thus, self-assembly modification for $Fe_3O_4$ NPs surface was confirmed by the result of FTIR. As illustrated in Fig. 2D, the Ni foam and $Fe_3O_4$-$Mn_3(PO_4)_2$@Ni foam (inset is $Fe_3O_4$ and $Fe_3O_4$-$Mn_3(PO_4)_2$ NPs) magnetic hysteresis loops at room temperature resembled mostly S-like curves. The exact potential was worked out to be 57.78 emu $g^{-1}$ for $Fe_3O_4$-$Mn_3(PO_4)_2$, slightly higher than 50.50 emu $g^{-1}$ for $Fe_3O_4$-$Mn_3(PO_4)_2$@Ni foam. Thus, the adequate magnetic force of the 3D hybrid foam could satisfy the demand of the electrode surface for rapid magnetic attraction.

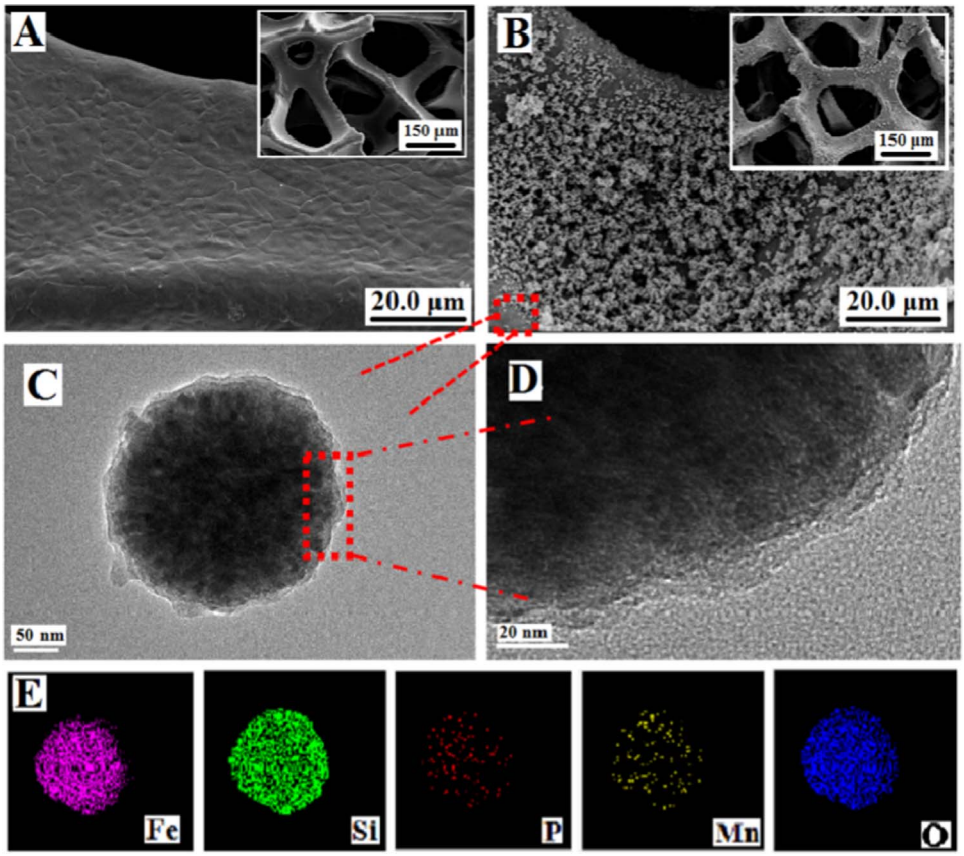


**Fig. 1.** SEM images of Ni foam (A) and $Fe_3O_4$-$Mn_3(PO_4)_2$@Ni foam (B); HETEM images (C and D) of $Fe_3O_4$-$Mn_3(PO_4)_2$ at 50 nm and 20 nm, respectively; (E) Element mapping of $Fe_3O_4$-$Mn_3(PO_4)_2$ NPs.

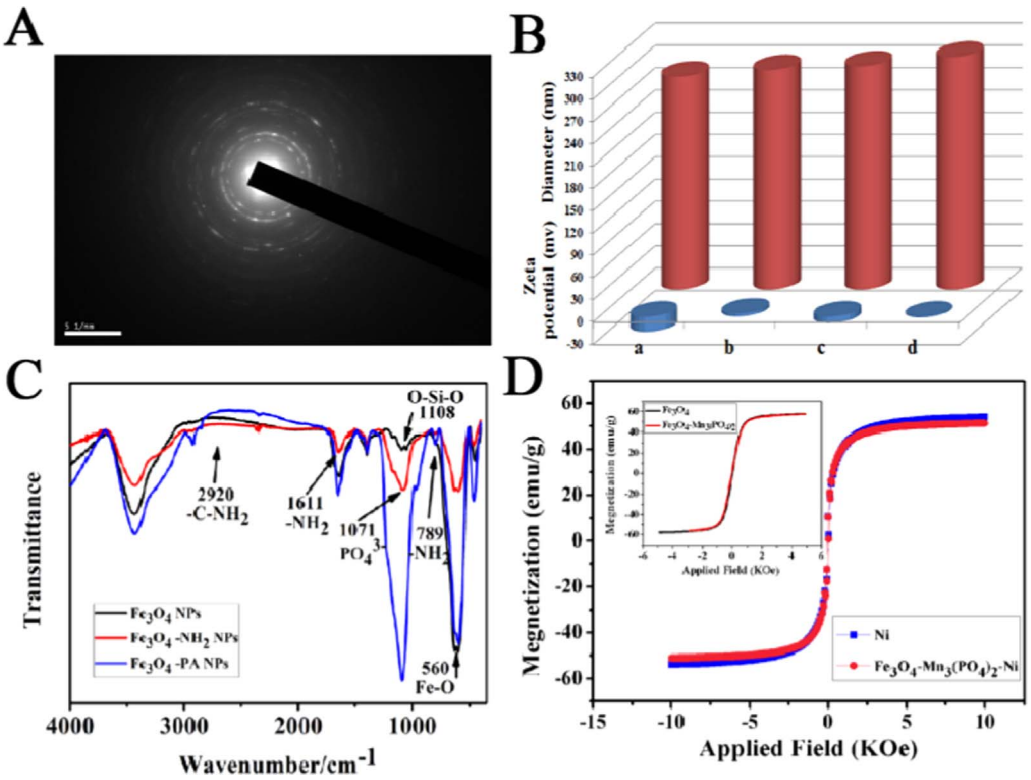


**Fig. 2.** (A) SAED patterns of $Fe_3O_4$-$Mn_3(PO_4)_2$ NPs; (B) Diameter (red) and zeta potential (blue) of $Fe_3O_4$ (a), $Fe_3O_4$-$NH_2$ (b), $Fe_3O_4$-PA (c) and $Fe_3O_4$-$Mn_3(PO_4)_2$ (d); (C) FTIR spectrum of various $Fe_3O_4$ NPs and (D) Magnetization curves of Ni foam and $Fe_3O_4$-$Mn_3(PO_4)_2$@Ni foam (inset is magnetization curves of $Fe_3O_4$ NPs and $Fe_3O_4$-$Mn_3(PO_4)_2$ NPs). (For interpretation of the references to color in this figure legend, the reader is referred to the web version of this article).

### 3.2. The captures cells on the 3D biointerface

For the purpose of in situ detection of $O_2^{\bullet -}$ that released from living cells, the attachment and growth of cells on the 3D sample were particularly important. As shown in Fig. 3, SEM and fluorescence microscopy were applied to evaluate the adhesion property of A549 cells on the surface of 3D hybrid foam. Results of MTT assays (Fig. S3, ESI) indicated that there were no clear cytotoxic effects for different samples

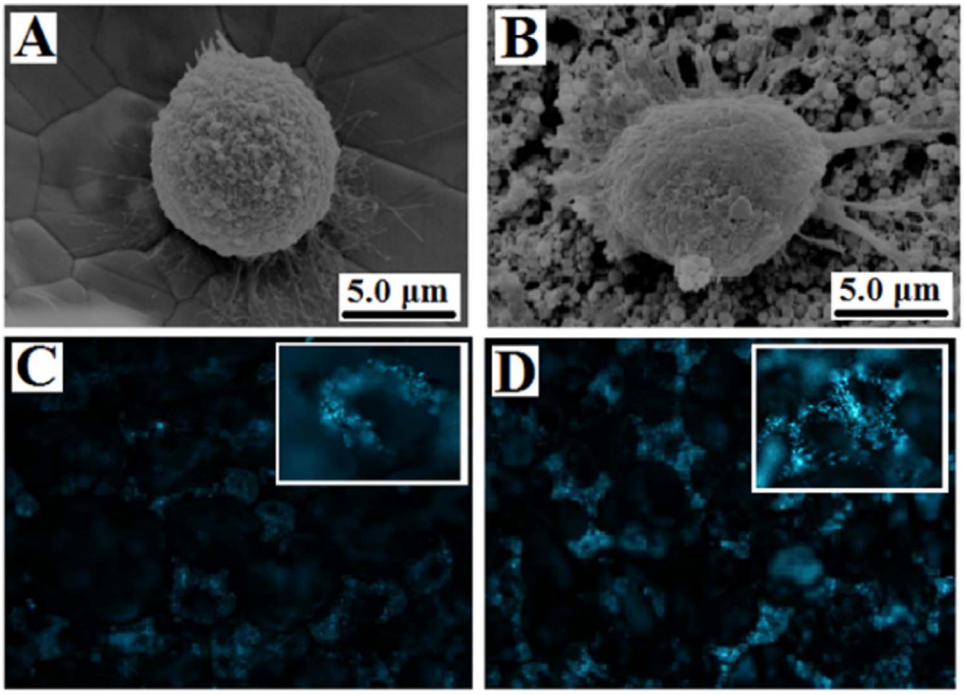


**Fig. 3.** SEM images of A549 cells cultured on (A) Ni foam and (B) $Fe_3O_4$-$Mn_3(PO_4)_2$@Ni foam; Fluorescence microscope images of cells cultured on (C) Ni foam and (D) $Fe_3O_4$-$Mn_3(PO_4)_2$@Ni foam (inset are partial magnification).

due to their good biocompatibility in cell ambience. Compared to these previous studies [49–51], the effect of cell adhesion was achieved just by the geometrical structure of this 3D $Fe_3O_4$-$Mn_3(PO_4)_2$@Ni foam we prepared, but not chemical or biochemical methods. Fig. 3A clearly displayed that few pseudopodia of a single cell could be found. In contrast, the good growth status of a single cell was emerged with presented many stretched pseudopodia (Fig. 3B), denoting that the cell adhesion behavior was further enhanced by incorporating $Fe_3O_4$-$Mn_3(PO_4)_2$ NPs onto the surface of Ni foam.

### 3.3. The electrochemical behavior of the 3D biosensor

Here the electrochemical biosensor was constructed through the magnetic attraction between $Fe_3O_4$-$Mn_3(PO_4)_2$ NPs and Ni foam in Fig. 4A, which was a simple and fast method to obtain the 3D biointerface for $O_2^{\bullet-}$ detection. During this response, $O_2^{\bullet-}$ catalyzed by $Mn_2^{+}$ in the PBS solution was alternated into $O_2$ and $H_2O_2$, whereas $MnO_2^{+}$ was reduced to $Mn_2^{+}$, and $O_2^{\bullet-}$ was oxidized to $O_2$, an outcome consistent with the reported finding [52]. The electrocatalytic properties of the as-prepared different samples modified MGCE were assessed toward in 1.0 μM $O_2^{\bullet-}$ at a scan rate of 100 mV $s^{-1}$ in the solution (pH = 7.4) by the CV and EIS curves (Fig. 4B, C). To comparison to the electrocatalytic performance of Ni foam-MGCE and $Fe_3O_4$-$Mn_3(PO_4)_2$@Ni foam-MGCE (Fig. 4B), $Fe_3O_4$-$Mn_3(PO_4)_2$@Ni foam-MGCE had obvious oxidation-reduction peaks, which may be ascribed to the catalytic action of the $Fe_3O_4$-$Mn_3(PO_4)_2$ capped on Ni foam in the presence of $O_2^{\bullet-}$. Fig. 4C was shown the Nyquist diagrams of bare MGCE (curve a), Ni foam-MGCE (curve b), and $Fe_3O_4$-$Mn_3(PO_4)_2$@Ni foam-MGCE (curve c). When the MGCE was covered by Ni foam, there existed a very small semi-circular domain, indicating that Ni foam possessed excellent conductivity. After $Fe_3O_4$-$Mn_3(PO_4)_2$@Ni foam was coated onto the MGCE, the semi-circular domain became enlarged due to the slightly weaker electrical conductivity of $Fe_3O_4$-$Mn_3(PO_4)_2$ NPs, which was also proved that the 3D biosensor was built successfully. Fig. 4C inset shows the detailed changes in the Rct value. The equivalent circuit of Nyquist diagrams for this biosensor we prepared was displayed in the inset of Fig. 4C involving charge-transfer resistance (Rct), Warburg impedance (Zw), solution resistance (Rs) and double layer capacitance (Cd) (Table S1). From Table S1, the charge-transfer resistances (Rct) of (a) bare MGCE; (b) Ni foam-MGCE and (c) $Fe_3O_4$-$Mn_3(PO_4)_2$@Ni foam-MGCE were calculated to be 237.6 Ω, 242.3 Ω and 542.0 Ω, respectively, which were consistent with the result of the Nyquist diagrams. The influence of scan rate on the electrochemical behavior of the 3D biosensor was monitored by CV. The peak currents (Ip) of the 3D biosensor were proportional to the scan rate as shown in Fig. S4, the results suggested the electrochemical reaction of as-prepared biosensor was a diffusion-controlled process.

### 3.4. Selectivity, sensitivity, stability, reusability and threshold of biosensor

The amperometric response of the 3D biosensor was characterized by injection continuously of $O_2^{\bullet-}$ (Fig. 5A). $Fe_3O_4$-$Mn_3(PO_4)_2$@Ni-MGCE had a broad linear response over the range from 0.04 to 2.44 μM with the correlation coefficient of 0.9972, which had wider linear range than those of some other modified electrodes and methods (Table S2). As shown in Fig. 5A, there was a similar linear relationship between the response current and $O_2^{\bullet-}$ concentration. It can be expressed as i (μA) = 0.03699–0.22814 C (μM) over the corresponding range with a detection limit of 0.0170 μM (S/N = 3). The detection limit was lower than those of some other modified electrodes (Table S3, ESI). As demonstrated in Fig. 5B, all interfering species tested, including 1.0 μM $O_2^{\bullet-}$, 5.0 μM Cys, 5.0 μM DA, 10 μM $H_2O_2$, 10 μM UA and 5.0 μM 18-crown-6, negligibly interfered with the 3D biosensor in response to 1 μM $O_2^{\bullet-}$, which was confirmed by statistical data (Fig. 5C). The stability of the 3D biosensor was monitored after fifteen days by being stored at room temperature, the current response (Fig. S5, ESI) was indicated no apparent change, whose stability better than those enzyme biosensors [53–55]. This above results clearly indicated that the as-prepared 3D biosensor was very accurate and reliable for evaluating the concentration of $O_2^{\bullet-}$ in complex samples. In order to investigate the reusability of this biosensor, the results of cyclic voltammetry for 20 cycles were detected in Fig. S6, which showed an almost overlap curves, indicating a good cycle reusability of this biosensor. The breakthrough concentration of $H_2O_2$, as a main interference, influenced the threshold of this system. The breakthrough concentration of $H_2O_2$ (threshold) was about 0.1 mM (Fig. S7, ESI). At this concentration of $H_2O_2$, a strong increase in the current was observed. If the threshold was exceeded which indicated the interfering substance hinder $O_2^{\bullet-}$

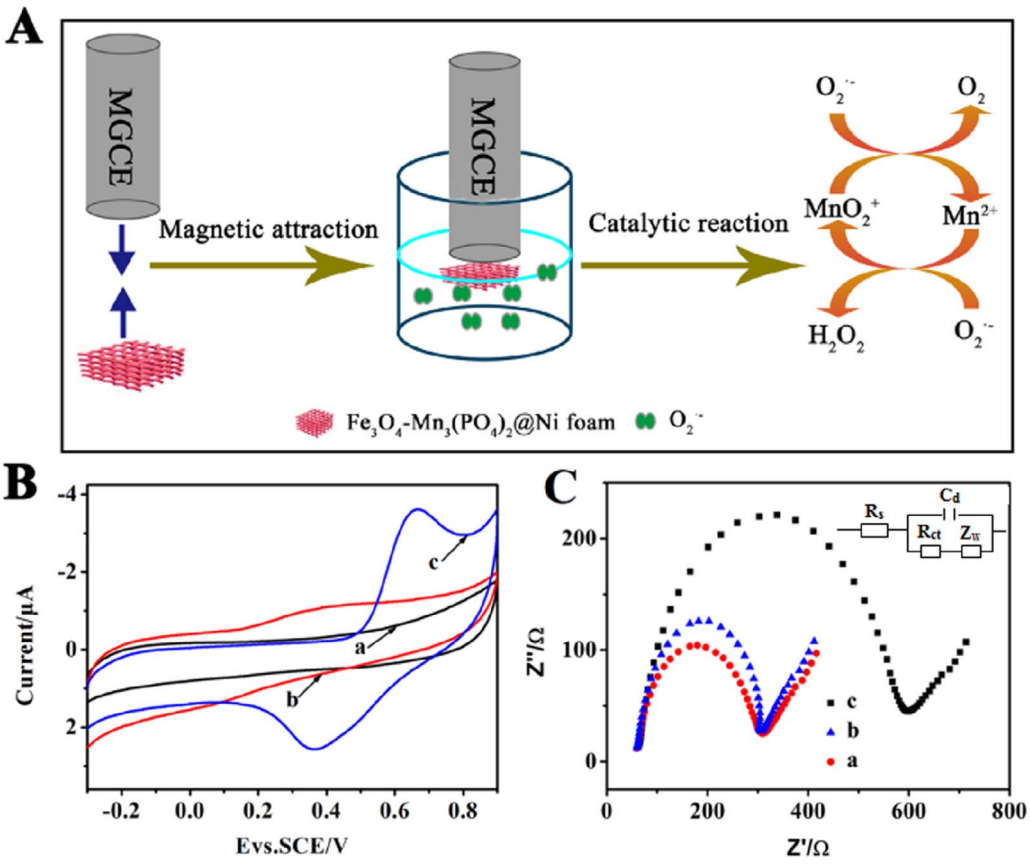


**Fig. 4.** (A) The construction of 3D biosensor for $O_2^{\cdot-}$ detection; (B) Cyclic voltammograms (CVs) and (C) Electrochemical Impedance Spectroscopy (EIS) of (a) bare MGCE; (b) Ni foam-MGCE and (c) $Fe_3O_4$-$Mn_3(PO_4)_2$@Ni foam-MGCE.

detection in this system.

### 3.5. Cell monitoring

Detection in situ of released $O_2^{\cdot-}$ from living cells grown on the proposed 3D hybrid biosensor was performed in Fig. 5D. In contrast to the samples in A549 cells suspension without PMA treatment (curve a), the sensor in 0.5 × $10^5$ cells $mL^{-1}$ suspension showed a crucially increased current response of 0.0033 μA at 484 mV (versus $Hg/Hg_2Cl_2$) upon injection of 4 μg $mL^{-1}$ PMA (curve b) [56], suggesting an

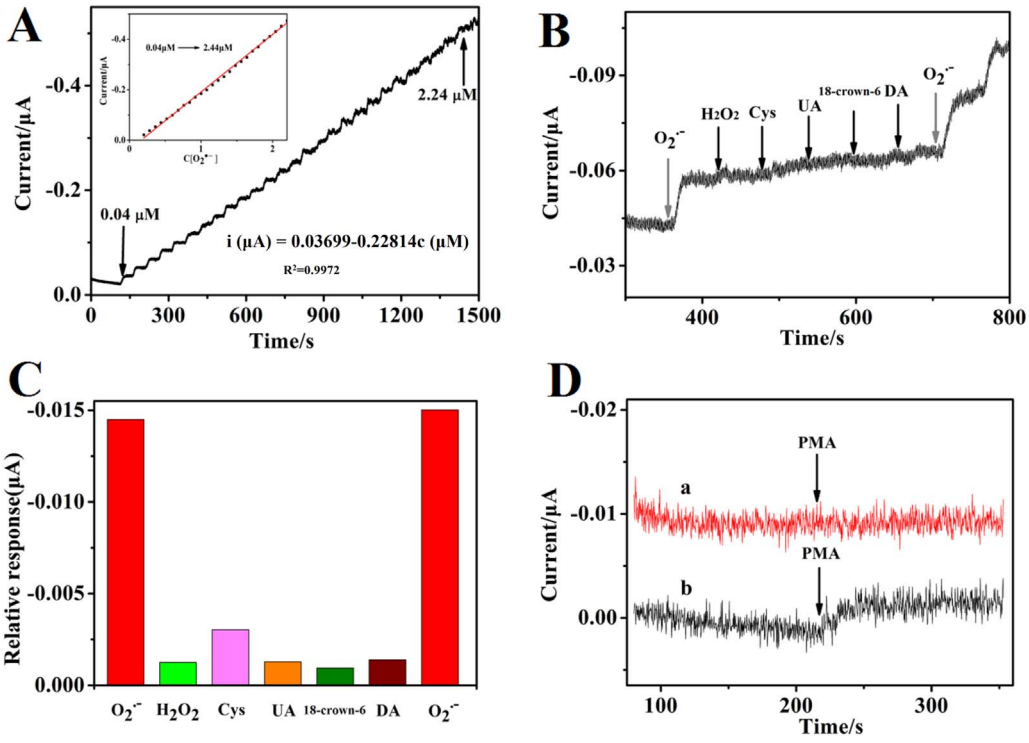


**Fig. 5.** (A) Typical amperometric response of $Fe_3O_4$-$Mn_3(PO_4)_2$@Ni-MGCE with successive addition of 10 μL, 0.03 μM $O_2^{\cdot-}$ solution. (inset shows corresponding calibration curves with $O_2^{\cdot-}$ concentration); (B) Interference test and (C) relative response of $Fe_3O_4$-$Mn_3(PO_4)_2$@Ni-MGCE; (D) Ampero metric response of $O_2^{\cdot-}$ release from the A549 cells by addition of PMA (a) absence and (b) presence of cells.

considerable release of $O_2^{\bullet -}$ provoked by the stimulant drug. The 0.1477 μM $O_2^{\bullet -}$ was released from 0.5 × $10^5$ cells $mL^{-1}$, according to the linear relationship in Fig. 5A. The calibration method for this biosensor was followed by the spectrophotometry in Fig. S8. The concentration of $O_2^{\bullet -}$ was determined by spectrophotometrically recording the absorbance of ferricytochrome c at 550 nm, and the average concentration of $O_2^{\bullet -}$ in 5 parallel experiments was 0.1459 μM. The 0.1477 μM $O_2^{\bullet -}$ was recorded by electrochemical method, and the relative error was 1.2%.

### 3.6. Accuracy and precision of biosensor

Real samples were analyzed by two detection methods which included electrochemical method and spectrophotometry. There were no significant difference between the above two methods, which indicated a good accuracy was achieved. The precision of this biosensor we obtained was evaluated by assaying current-time curve of $Fe_3O_4$-$Mn_3(PO_4)_2$@Ni foam-MGCE upon addition of $O_2^{\bullet -}$ (0.12 μM) for three replicate determinations in Fig. S9. According to the linear relationship between the response current and $O_2^{\bullet -}$ concentration (i (μA) = 0.03699–0.22814 C (μM)) in Fig. 5A, the response current was 0.09532 μA, 0.09613 μA, 0.09467 μA at the same concentration (0.12 μM) of $O_2^{\bullet -}$, respectively. The R.S.D. was found to be 0.8%, indicating acceptable reproducibility.

## 4. Conclusion

Inspired by the adhesion of mussels, $Fe_3O_4$-$Mn_3(PO_4)_2$ synthesized by surface self-assembly technology, were directly anchored on nickel foam to fabricate 3D micro/nano-biointerfaces. Compared to these existing $O_2^{\bullet -}$ detection methods, we designed and prepared a novel biosensor with a micro/nano-biointerface of $Fe_3O_4$-$Mn_3(PO_3)_2$@Ni foam, which offered a 3D living environment for real cell, which exhibited good matching with cancer cells and enhanced the topographical interaction between cells and substrate, resulting in the improvement of cell-capture capability that useful for further electron transfer efficiency. Therefore, this work has potential to construct a novel sensing platform about living cell-based biological assays.

## Acknowledgment

The work was supported by Jiangsu Collaborative Innovation Center of Biomedical Functional Materials, National Natural Science Foundation of China (51641104, 21603105, 21571104), Medical Science and Technology Development Foundation, Nanjing Department of Health (JQX14002), Social Development Project of Jiangsu (BE2015603), Jiangsu Key Technology RD Program (BE2016010), Major projects of Natural Sciences of University in Jiangsu Province (14KJA150006), the Priority Academic Program Development of Jiangsu Higher Education Institution, and Huaian Key Research and Development Program (HAG201621).

## Notes

The authors declare no competing financial interest.

## Appendix A. Supporting information

Supplementary data associated with this article can be found in the online version at http://dx.doi.org/10.1016/j.talanta.2017.10.054.

## References

[1] J.E. Klaunig, L.M. Kamendulis, The role of oxidative stress in carcinogenesis, Annu. Rev. Pharmacol. Toxicol. 44 (2004) 239–267.
[2] E.D. Hall, J.M. Braughler, Central nervous systems trauma and stroke: I. Biochemical considerations for oxygen radical formation and lipid peroxidation, Free Radic. Biol. Med. 6 (1989) 289–301.
[3] A. Vanella, C.D. Giacomo, V. Sorrenti, A. Russo, C. Castorina, A. Campisi, M. Renis, J. Perez-Polo, Free radical scavenger depletion in post-ischemic reperfusion brain damage, Neurochem. Res. 18 (1993) 1337–1340.
[4] D.C. Wallace, Mitochondrial diseases in man and mouse, Science 283 (1999) 1482–1488.
[5] B.N. Ames, M.K. Shigenaga, T.M. Hagen, Oxidants, antioxidants, and the degenerative diseases of aging, Proc. Natl. Acad. Sci. USA 90 (1993) 7915–7922.
[6] S. Liu, J.P. Xing, Z. Zheng, F.R. Song, Z.Q. Liu, S.Y. Liu, Ultrahigh performance liquid chromatography–triple quadrupole mass spectrometry inhibitors fishing assay: a novel method for simultaneously screening of xanthine oxidase inhibitor and superoxide anion scavenger in a single analysis, Anal. Chim. Acta 715 (2012) 64–70.
[7] Q. Wang, X.Q. Yang, D.Y. Qu, In situ ESR spectro-electrochemical investigation of the superoxide anion radical during the electrochemical $O_2$ reduction reaction in aprotic electrolyte, Carbon 61 (2013) 336–341.
[8] P. Pieta, A. Petr, W. Kutner, L. Dunsch, In situ ESR spectroscopic evidence of the spin-trapped superoxide radical, $O_2^{\bullet -}$, electrochemically generated in DMSO at room temperature, Electrochim. Acta 53 (2008) 3412–3415.
[9] X. Gao, C.Q. Ding, A.W. Zhu, Y. Tian, Carbon-dot-based ratiometric fluorescent probe for imaging and biosensing of superoxide anion in live cells, Anal. Chem. 86 (2014) 7071–7078.
[10] X.R. Li, B. Wang, J.J. Xu, H.Y. Chen, In vitro detection of superoxide anions released from cancer cells based on potassium-doped carbon nanotubes–ionic liquid composite gels, Nanoscale 3 (2011) 5026–5033.
[11] W.T. Li, Y.S. Li, Y.K. Wu, J.F. Liao, T.T. Qi, H. Li, J. Li, X.N. Zhang, Z.Y. Qian, A nonenzymatic electrochemical immunosensor for ultrasensitive detection of tumor biomarkers based on palladium nanoparticles conjugated reduced graphene nanosheets, J. Biomed. Nanotechnol. 11 (2015) 2050–2056.
[12] T. Tachikawa, N. Wang, S. Yamashita, S.C. Cui, T. Majima, Design of a highly sensitive fluorescent probe for interfacial electron transfer on a $TiO_2$ surface, Angew. Chem. Int. Ed. 49 (2010) 8593–8597.
[13] A. Umar, M.S. Chauhan, S. Chauhan, R. Kumar, P. Sharma, K.J. Tomar, R. Wahab, A. Al-Hajry, D. Singh, Applications of ZnO nanoflowers as antimicrobial agents for Escherichia coli and enzyme-free glucose sensor, J. Biomed. Nanotechnol. 9 (2013) 1794–1802.
[14] R.R. Huang, Z.J. Xi, N.Y. He, Applications of aptamers for chemistry analysis, medicine and food security, Sci. China Chem. 58 (2015) 1122–1130.
[15] C.J. McNeil, K.R. Greenough, P.A. Weeks, C.H. Self, J.M. Cooper, Electrochemical sensors for direct reagentless measurement of superoxide production by human neutrophils, Free Radic. Res. Commun. 17 (1992) 399–406.
[16] V. Lvovich, A. Scheeline, Amperometric sensors for simultaneous superoxide and hydrogen peroxide detection, Anal. Chem. 69 (1997) 454–462.
[17] J. Chen, U. Wollenberger, F. Lisdat, B.X. Ge, F.W. Scheller, Superoxide sensor based on hemin modified electrode, Sens. Actuators B-Chem. 70 (2000) 115–120.
[18] Z. Deng, Q. Rui, X. Yin, H. Liu, Y. Tian, In vivo detection of superoxide anion in bean sprout based on ZnO nanodisks with facilitated activity for direct electron transfer of superoxide dismutase, Anal. Chem. 80 (2008) 5839–5846.
[19] X.H. Shen, Q. Wang, Y.H. Liu, W.X. Xue, L. Ma, S.H. Feng, M.M. Wan, F.H. Wang, C. Mao, Manganese phosphate self-assembled nanoparticle surface and its application for superoxide anion detection, Sci. Rep. 6 (2016) 28989.
[20] X.L. Liu, L. Chen, H.L. Liu, G.P. Yang, C. Zhang, D. Han, S.T. Wang, L. Jiang, Bioinspired soft polystyrene nanotube substrate for rapid and highly efficient breast cancer-cell capture, NPG Asia Mater. 5 (2013) e63.
[21] W. Kim, J.K. Ng, M.E. Kunitake, B.R. Conklin, P.D. Yang, Interfacing silicon nanowires with mammalian cells, J. Am. Chem. Soc. 129 (2007) 7228–7229.
[22] H.L. Liu, Y.Y. Li, K. Sun, J.B. Fan, P.C. Zhang, J.X. Meng, S.T. Wang, L. Jiang, Dual-responsive surfaces modified with phenylboronic acid-containing polymer brush to reversibly capture and release cancer cells, J. Am. Chem. Soc. 135 (2013) 7603–7609.
[23] L. Chen, X.L. Liu, B. Su, J. Li, L. Jiang, D. Han, S.T. Wang, Dual-responsive surfaces modified with phenylboronic acid-containing polymer brush to reversibly capture and release cancer cells, Adv. Mater. 23 (2011) 4376–4380.
[24] Y. Chen, X. Zhang, P. Yu, Y. Ma, Electrophoretic deposition of graphene nanosheets on nickel foams for electrochemical capacitors, J. Power Sources 9 (2010) 3031–3035.
[25] Z. Chen, W. Ren, L. Gao, B. Liu, S. Pei, H.M. Cheng, Three-dimensional flexible and conductive interconnected graphene networks grown by chemical vapour deposition, Nat. Mater. 6 (2011) 424–428.
[26] H.W. Yang, M. Liu, B.C. Zhou, Y. Deng, N.Y. He, H.S. Jiang, Y.F. Guo, G.Q. Lan, Q.Y. Jiang, X.R. Yang, Z.Y. Li, Chemiluminescent detection for estimating relative copy numbers of porcine endogenous retrovirus proviruses from chinese minipigs based on magnetic nanoparticles, J. Nanosci. Nanotechnol. 16 (2016) 6505–6510.
[27] Z.H. Xu, C.X. Li, X.J. Kang, D.M. Yang, P.P. Yang, Z.Y. Hou, J. Lin, Synthesis of a multifunctional nanocomposite with magnetic, mesoporous, and near-IR absorption properties, J. Phys. Chem. C 114 (2010) 16343–16350.
[28] Z. Ali, W.B. Liang, L. Jin, Y.J. Tang, X.B. Mou, M.A.A. Shah, H.W. Yang, Y. Deng, N.Y. He, Z.Y. Li, Development of magnetic nanoparticles based nucleic acid extraction method and application in hepatitis C virus chemiluminescent detection, Sci. Adv. Mater. 7 (2015) 1233–1240.
[29] Y.H. Deng, D.W. Qi, C.H. Deng, X.M. Zhang, D.Y. Zhao, Superparamagnetic high-magnetization microspheres with an $Fe_3O_4$@$SiO_2$ core and perpendicularly aligned mesoporous $SiO_2$ shell for removal of microcystins, J. Am. Chem. Soc. 130 (2008) 28–29.
[30] H.R. Jiang, X. Zeng, Z.J. Xi, M. Liu, C.Y. Li, Z.Y. Li, L. Jin, Z.F. Wang, Y. Deng,

N.Y. He, Improvement on controllable fabrication of streptavidin-modified three-layer core–shell $Fe_3O_4$@$SiO_2$@Au magnetic nanocomposites with low fluorescence background, J. Biomed. Nanotechnol. 9 (2013) 674–684.
[31] W.B. Zhao, K. Wang, Y. Wei, Y.H. Ma, L.L. Liu, X.H. Huang, Laccase biosensor based on phytic acid modification of nanostructured $SiO_2$ surface for sensitive detection of dopamine, Langmuir 30 (2014) 11131–11137.
[32] J. Fan, H.W. Yang, M. Liu, D. Wu, H.R. Jiang, X. Zeng, S. Elingarami, Z.Y. Li, S. Li, H.N. Liu, N.Y. He, Fluorescent quantification of DNA based on core–shell $Fe_3O_4$@$SiO_2$@Au nanocomposites and multiplex ligation-dependent probe amplification, J. Nanosci. Nanotechnol. 15 (2015) 1123–1129.
[33] L. Haeshin, S.M. Dellatore, W.M. Miller, P.B. Messersmith, mussel-inspired surface chemistry for multifunctional coatings, Science 318 (2007) 426–430.
[34] H. Lee, N.F. Scherer, P.B. Messersmith, Single-molecule mechanics of mussel adhesion, Proc. Natl. Acad. Sci. USA 103 (2006) 12999–13003.
[35] K. Thandavan, S. Gandhi, S. Sethuraman, J.B.B. Rayappan, U.M. Krishnan, A novel nano-interfaced superoxide biosensor, Sens. Actuatos B-Chem. 176 (2013) 884–892.
[36] F. Tang, X.Y. Wang, X.J. Xu, L.D. Li, Phytic acid doped nanoparticles for green anticorrosion coatings, Colloid Surf. A 369 (2010) 101–105.
[37] C. Sun, L.B. Chen, F.J. Xu, P.Y. Zhu, J.F. Luan, C. Mao, J. Shen, Hemocompatible and antibiofouling PU-F127 nanospheres platform for application to glucose detection in whole blood, J. Mater. Chem. B 1 (2013) 801–809.
[38] S.K. Maji, S. Sreejith, A.K. Mandal, X. Ma, Y.L. Zhao, Immobilizing gold nanoparticles in mesoporous silica covered reduced graphene oxide: a hybrid material for cancer cell detection through hydrogen peroxide sensing, ACS Appl. Mater. Interfaces 6 (2014) 13648–13656.
[39] H.M. Cao, D.P. Yang, D.X. Ye, X.X. Zhang, X.E. Fang, S. Zhang, B.H. Liu, J.L. Kong, Protein-inorganic hybrid nanoflowers as ultrasensitive electrochemical cytosensing Interfaces for evaluation of cell surface sialic acid, Biosens. Bioelectron. 68 (2015) 329–335.
[40] V. Aravindan, K. Karthikeyan, K.S. Kang, W.S. Yoon, W.S. Kim, Y.S. Lee, Influence of carbon towards improved lithium storage properties of $Li_2MnSiO_4$ cathodes, J. Mater. Chem. 21 (2011) 2470–2475.
[41] C. Sun, X.B. Wang, M. Zhou, Y.L. Ni, C. Mao, X.H. Huang, J. Shen, An innovative glucose biosensor using antibiofouling Au-F127 nanospheres, J. Biomed. Nanotechnol. 9 (2013) 825–832.
[42] J. Mohapatra, A. Mitra, D. Bahadur, M. Aslam, Surface controlled synthesis of $MFe_2O_4$ (M= Mn, Fe, Co, Ni and Zn) nanoparticles and their magnetic characteristics, CrystEngComm 15 (2013) 524–532.
[43] F. Tang, X.Y. Wang, X.J. Xu, L.D. Li, Phytic acid doped nanoparticles for green anticorrosion coatings, Colloid Surf. A 369 (2010) 101–105.
[44] R.P. Bagwe, L.R. Hilliard, W. Tan, Surface modifcation of silica nanoparticles to reduce aggregation and nonspecifc binding, Langmuir 22 (2006) 4357–4362.
[45] J. Mohapatra, A. Mitra, H. Tyagi, D. Bahadur, M. Aslam, Iron oxide nanorods as high-performance magnetic resonance imaging contrast agents, Nanoscale 7 (2015) 9174–9184.
[46] V.K.S. Hsiao, J.R. Waldeisen, Y.B. Zheng, P.F. Lloyd, T.J. Bunning, T.J. Huang, Aminopropyltriethoxysilane (APTES)-functionalized nanoporous polymeric gratings: fabrication and application in biosensing, J. Mater. Chem. 17 (2007) 4896–4901.
[47] W.B. Zhao, Y.L. Ni, Q.S. Zhu, R.J. Fu, X.H. Huang, J. Shen, Innovative biocompatible nanospheres as biomimetic platform for electrochemical glucose biosensor, Biosens. Bioelectron. 44 (2013) 1–5.
[48] J. Dong, Y. Wen, Y. Miao, Z.J. Xie, Z.R. Zhang, H.F. Yang, A nanoporous zirconium phytate film for immobilization of redox protein and the direct electrochemical biosensor, Sensor, Actuators B-Chem. 150 (2010) 141–147.
[49] C.X. Guo, X.T. Zheng, Z.S. Lu, X.W. Lou, C.M. Li, Biointerface by cell growth on layered graphene-artificial peroxidase-protein nanostructure for in situ quantitative molecular detection, Adv. Mater. 22 (2010) 5164–5167.
[50] C.X. Guo, S.R. Ng, S.Y. Khoo, X. Zheng, P. Chen, C.M. Li, RGD-peptide functionalized graphene biomimetic live-cell sensor for real-time detection of nitric oxide molecules, ACS Nano 6 (2012) 6944–6951.
[51] H. Asakawa, K. Mochitate, T. Haruyama, Seamless signal transduction from live cells to an no sensor via a cell-adhesive sensing matrix, Anal. Chem. 80 (2008) 1505–1511.
[52] J.Q. Zhou, Y.P. Luo, A.W. Zhu, Y. Liu, Z.R. Zhu, Y. Tian, A reliable and durable approach for real-time determination of cellular superoxide anion based on biomimetic superoxide dismutase stabilized by a zeolite, Analyst 136 (2011) 1594–1598.
[53] X. Zhu, X.H. Niu, H.L. Zhao, J. Tang, M.B. Lan, Immobilization of superoxide dismutase on Pt-Pd/MWCNTs hybrid modified electrode surface for superoxide anion detection, Biosens. Bioelectron. 67 (2015) 79–85.
[54] L. Wang, W. Wen, H.Y. Xiong, X.H. Zhang, H.S. Gu, S.F. Wang, A novel amperometric biosensor for superoxide anion based on superoxide dismutase immobilized on gold nanoparticle-chitosan-ionic liquid biocomposite film, Anal. Chim. Acta 758 (2013) 66–71.
[55] H.Q. Liu, Y. Tian, P.P. Xia, Pyramidal, rodlike, spherical gold nanostructures for direct electron transfer of copper, zincsuperoxide dismutase: application to superoxide anion biosensors, Langmuir 24 (2008) 6359–6366.
[56] Y.P. Luo, G.Q. Hu, A.W. Zhu, B. Kong, Z. Wang, C.Y. Liu, Y. Tian, A biomimetic sensor for the determination of extracellular $O_2^{\cdot -}$ using synthesized Mn-TPAA on $TiO_2$ nanoneedle film, Biosens. Bioelectron. 29 (2011) 189–194.